Supplemental Information for

Electron-phonon coupling dictates electron mean free paths and negative thermal diffusion in metals

*Pravin Karna, Md. Rafiqul Islam, Eric R Hoglund, Patrick E. Hopkins, and Ashutosh Giri**

S1. Experimental Setup and Thin Film Charecterization

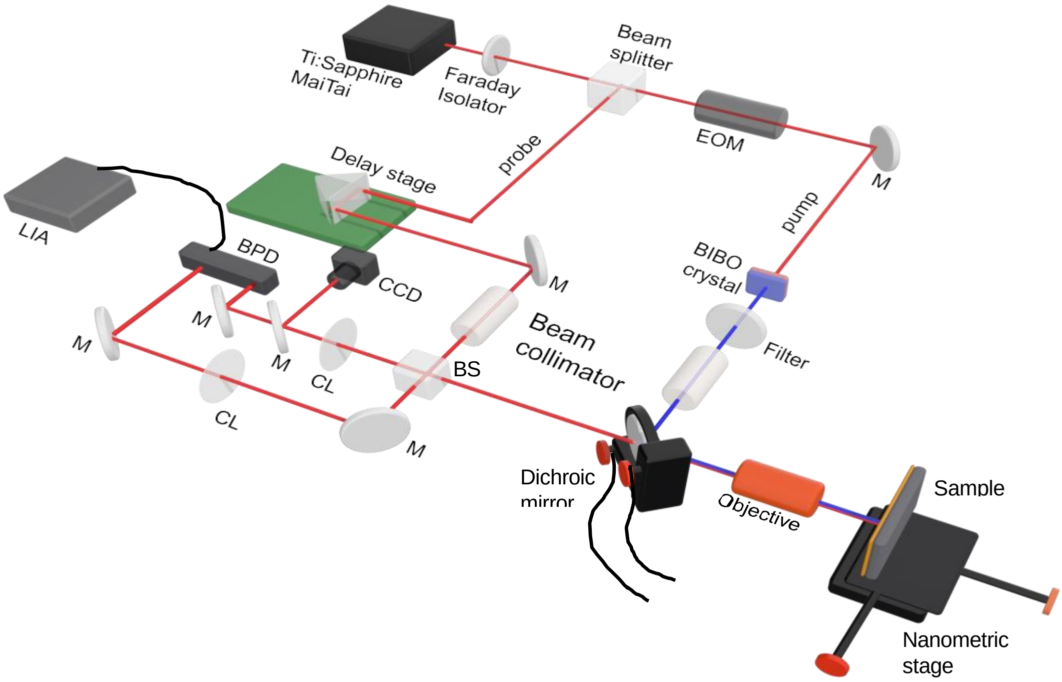

Figure S1: Schematic of our home-built ultrafast thermoreflectance setup. M denotes mirror, CL represents converging lens, CCD is for charged coupled device, BPD is balanced photo diode, EOM is electro-optic modulator, BS stands for beam splitter and LIA represents lock-in amplifier.

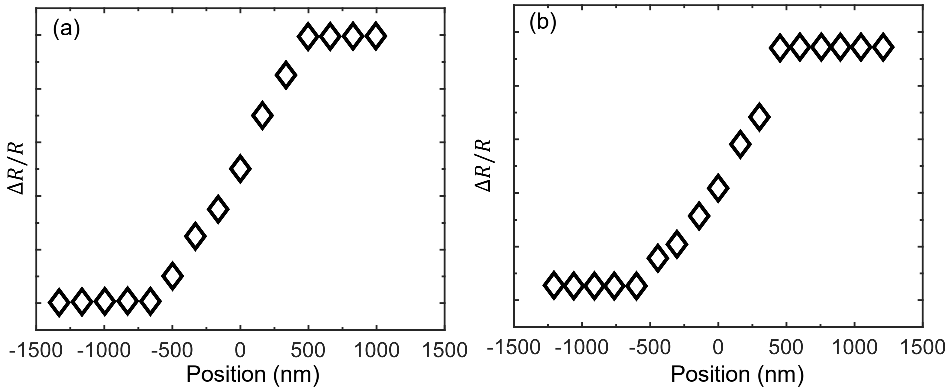

Figure S2: Pump and probe spot sizes carried out using knife edge measurements with our nano-metric piezo-stage.

In the knife edge measurement, we utilize a glass slide as the knife specimen, on top of which a thin layer of gold is deposited. The purpose of this gold film is to determine the focal point of both the pump and the probe beams through the reflection observed in our CCD camera. To quantify the focal diameter of the pump and the probe accurately, a photodiode placed behind the knife specimen is connected to an oscilloscope. Additionally, nanometric resolution is achieved using piezo-stage to measure the spot sizes of the pump and probe precisely. Multiple measurements are conducted to determine the exact focal diameters of both the pump and the probe, ensuring reliable results. The measurements are taken at a spatial resolution of ~20 nm.

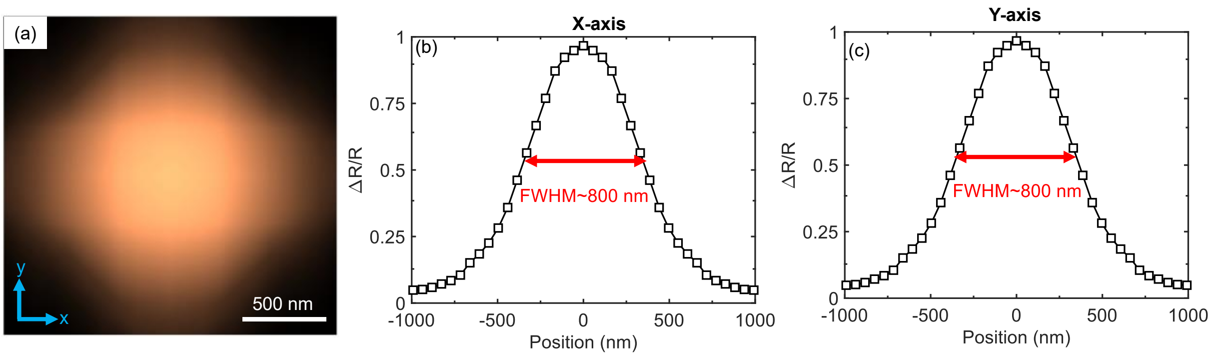

Figure S3: (a) 2D scan of $\Delta R/R$ at the peak signal for our gold thin film. The full-width at half maximum obtained at zero pump-probe delay is ~800 nm when scanned along (b) x-axis and (c) y-axis.

We scan the laser spot along both x- and y-axis to ascertain the Gaussian shape of our laser spot with the help of our nanometric stage. We show that our laser spot is indeed circular and the full width at half maximum (FWHM) along the various directions is ~800nm at 0 ps time delay (or at the peak signal obtained) performed for our gold thin film. The increase in the FWHM from the spot size (~650 nm) is attributed to spatial heat diffusion at the peak signal as also reported in previous studies.[1–3]

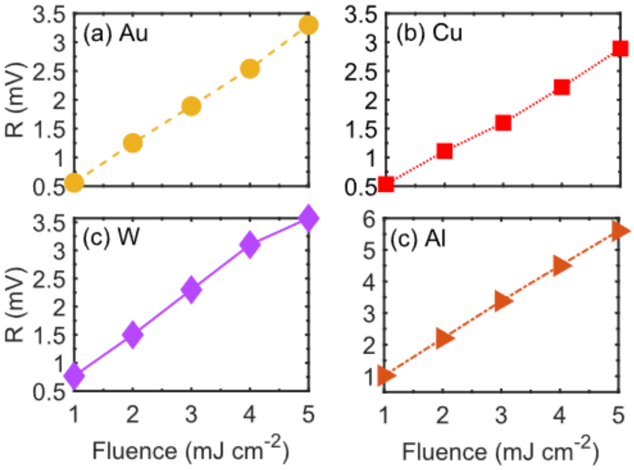

Figure S4: Variation of the peak reflectivity signal at 0 ps time delay with increase in pump fluence. The graph suggests that the fluences used for the measurement in this work lies in the linear regime of variation of reflectivity signal with pump fluences.

We also measure the variation of the peak reflectivity signal at 0 ps time delay with increase in pump fluence for all four metallic films. We observe that the range of pump fluence used in this study lies in the linear regime of increase in signal with fluence for all the four films.

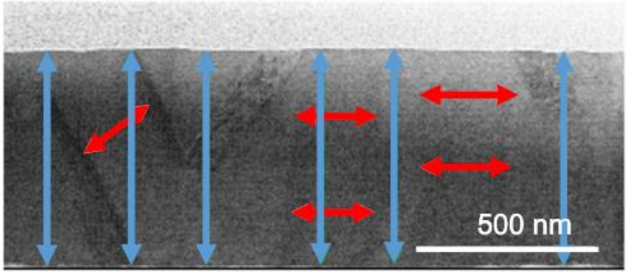

Figure S5: TEM micrographs of as-deposited Cu films. The blue arrows indicate the thickness of the copper film. The red arrows denote the region between grain boundaries indicating the polycrystalline nature of the thin films.

We use Transmission Electron Microscopy (TEM) to analyze the deposited thin film. The samples for the TEM analysis are prepared by using Thermo Fisher Helios or an FEI Nova 600 nanolab Dual Beam FIB. We reduce the cross-section to 50 nm or less by milling them. To prevent any potential damage from the gallium ion beam on thin cross sections, we use a platinum protective layer on Cu films. We capture the HRTEM images using a FEI Titam and double tilt stage at 300 kV. From our analysis we find that the grain size in the as deposited Cu film is approximately ~223.21±19.3 nm. The grain sizes are substantially greater than the average mean free path of electrons in copper.

S2. Comparison of thermoreflectance signal for different metals

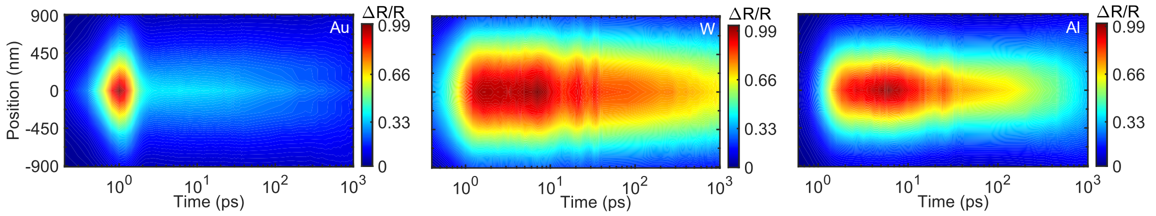

Figure S6: Contours showing spatiotempoaral variation of the thermoreflectance signals taken with our ultrafast pump-probe offset technique for Au, W and Al.

We compare the thermoreflectance signal for Au, W and Al as shown in Fig. S6. For Au, the thermoreflectance signal rises rapidly before decreasing to a significantly lower level. The rise in signal is driven by elevated electron temperatures, after which coupling of electrons with the cooler lattice leads to a reduction in the thermoreflectance signal. In contrast, the thermoreflectance for W and Al are very different without the features of the photo-excited electron relaxation as observed for Au and Cu. We also observe 'ripples' in the thermoreflectance for W and Al, which are indicative of a strain wave propagating in the thinner film.[4]

S3. General diffusion model

The slope of full-width at half maximum squared (σ^2) versus time is used to approximately calculate the diffusion coefficient or diffusivity. The absorbed laser power at the sample is assumed to have a Gaussian energy distribution, u(x, t = 0) ∝ exp($-4\ln 2|x^2|/\sigma^2$), where $x \epsilon R^n$ (n=1,2 or 3, spatial dimensions) and u evolves according to the heat diffusion equation,[5] and is used to calculate the time-dependent diffusivity as,

$$\frac{\partial u(x,t)}{\partial t} = D(t)\nabla^2 u(x,t). \tag{S1}$$

Alternatively, the heat equation can also be cast with a decay rate $\Gamma=1/\tau$,

$$\frac{\partial u(x,t)}{\partial t} = D(t)\nabla^2 u(x,t) - \Gamma u(x,t). \tag{S2}$$

The solutions for Eq. S1 and Eq. S2 in terms of u(x, t) are spatially gaussian and temporally decaying in nature. The relationship between the diffusivity and time dependent σ^2 is given by,

$$\frac{\partial \sigma^2(t)}{\partial t} = 16\ln(2)\, D(t)\ . \tag{S3}$$

Eq. S3 is a more generalized equation for a common time-independent diffusion coefficient D, given as $\sigma^2(t) = \sigma^2(t) + 2Dt$.

S4. Measurement of electron mean free path

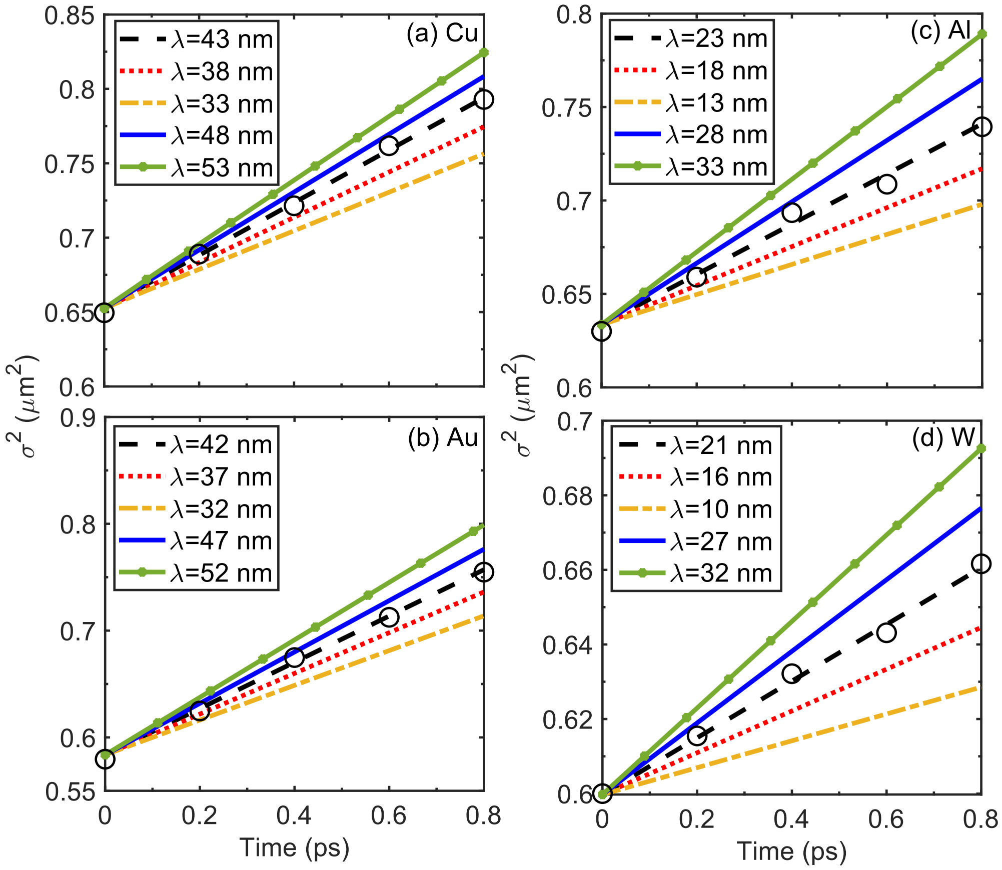

Figure S7: Fitting the initial fast rise of σ^2 with varying slopes (dictated by Λ) for (a) Cu, (b) Au, (c) Al and (d) W. The different lines show the sensitivity of Λ to the change in slope of initial fast region immediately after the laser excitation. This shows that we can accurately measure (within ~15% uncertainties as determined by 95% confidence interval fits) Λ from the fast diffusion regime in our spatially resolved pump-probe measurements.

We measure the average mean free paths (Λ) of electrons for four different metals, namely Au, Cu, Al, and W immediately after laser excitation with our ultrafast super-resolution thermoreflectance microscopy. We calculate the Λ of the electrons from the initial fast diffusion regime using the relation $\Lambda = 3D/v_{\mathrm{F}}$, where D is the electron diffusivity in the initial fast region, and v_{F} is the Fermi velocity of the electrons determined from our first-principles calculations. We also establish the sensitivity of our measurements by varying the slope of the initial fast diffusion region by changing the Λ. As shown in Fig. S7, uncertainties of ~15% can provide good fits to the experimental data in the least square sense (with 95% confidence levels). From our measurements, we calculate the Λ of electrons in Cu, Au, Al and W to be 43±6.5 nm, 42±6.5 nm, 23±3.5 nm, and 21 ±3.5 nm, respectively. Our measurements are consistent with our first-principles calculations listed in Table I. Moreover, our results also agree with prior theoretical and DFT calculations that report Λ values of 39.9 nm for Cu,[6,7] 37.7 nm for Au,[6,7] 18.9 nm for Al [6,7] and 18 nm for W.[8]

S5. Two-Temperature Model

We utilize the well-established two-temperature model to provide insights into the spatiotemporal profiles of the electron and phonon temperatures.[9,10] The temporal and spatial dependency of electron temperature T_e and the phonon temperature $T_\mathrm{p}$is given by the coupled differential equations,

$$C_\mathrm{e}(T_\mathrm{e})\frac{\partial \mathrm{T}_e}{\partial t} = \nabla\cdot(\kappa_\mathrm{e}\nabla T_\mathrm{e}) - G\left(T_\mathrm{e}-T_\mathrm{p}\right) + S(r,t), \tag{S4}$$

$$C_\mathrm{p}\left(T_\mathrm{p}\right)\frac{\partial \mathrm{T}_p}{\partial t} = \nabla\cdot\left(\kappa_\mathrm{p}\nabla T_\mathrm{p}\right) - G\left(T_\mathrm{e}-T_\mathrm{p}\right).$$

where C_e is the electron heat capacity, $C_\mathrm{p}$is the phonon heat capacity, κ_e is the electron thermal conductivity, $\kappa_\mathrm{p}$is the phonon heat capacity, G is the electron-phonon coupling coefficient, $S(r,t)$, is the source term. T_e and T_p represent the electron and phonon temperature, respectively. For Cu, $C_\mathrm{e}(T_\mathrm{e})$= γ T_e, γ =96.8 J m^{-3} K^{-2}, γ is the Sommerfield coefficient for electron heat capacity;[11] C_p= 3.45× 10^{6} J m^{-3} K^{-1} is the phonon heat capacity;[12] κ_e=401 W m^{-1} K^{-1} is the electronic thermal conductivity;[12] κ_p= 7.25 W m^{-1} K^{-1} is the phonon thermal conductivity;[13] G =8× 10^{16} W m^{-3} K^{-1} is the electron-phonon coupling coefficient.[14]

For W, $C_\mathrm{e}(T_\mathrm{e})$= γ T_e, γ =137.3 J m^{-3} K^{-2}, γ is the Sommerfield coefficient for electronic heat capacity;[11] C_p= 2.58× 10^{6} J m^{-3} K^{-1} is the phonon heat capacity;[12], κ_e=140 W m^{-1} K^{-1} is the electron thermal conductivity;[15], κ_p= 46 W m^{-1} K^{-1} is the phonon thermal conductivity;[15] G =2× 10^{17} W m^{-3} K^{-1} is the electron-phonon coupling coefficient.[11]

The term $\mathrm{S}(\mathrm{r},\mathrm{t})$ in Eq.~4 is the laser source term and is given by,

$$\mathrm{S}(\mathrm{r},\mathrm{t}) = \frac{(1-R)F}{d}\exp\left(-4\ln(2)\frac{x^2}{\sigma_\mathrm{pump}^2}\right)\frac{1}{t_\mathrm{pump}} \tag{S5}$$

$$\sqrt{\frac{4\ln(2)}{\pi}}\exp\left[-4\ln(2)\left(\frac{\left(t-2\left(t_\mathrm{pump}\right)\right)^2}{t_\mathrm{pump}^2}\right)\right].$$

where, F is the fluence of the laser, R is the reflectivity of the thin film, d is the optical penetration depth, $\sigma_\mathrm{pump}$is the spatial full-width half maximum of the pump pulse, and t_pump is the pulse duration.

The photo-excited electron transport and its cooling mechanism for both Cu and W are shown in Fig. S8. The yellow and cyan region of the figure represent the electronic and lattice subsystems, respectively. Immediately after the laser excitation, the electrons attain an extremely high temperature and start to cool through electron-phonon coupling, thus heating up the lattice. The electrons and the lattice subsequently attain thermal equilibrium. The time duration required for the electron and lattice to attain thermal equilibrium is dictated by the electron-phonon coupling factor. For Cu, the electron and phonon attain equilibrium only after ∼5 ps, while for tungsten the equilibrium is obtained after ∼3 ps. We also see that the lattice temperature goes higher than that of the electron temperature at long time scales, after the electron and the phonons have coupled together. This explains the negative peak value of the electron-phonon coupling term, A_1, that we calculate from the two-temperature picture at longer time scales as we discuss more below.

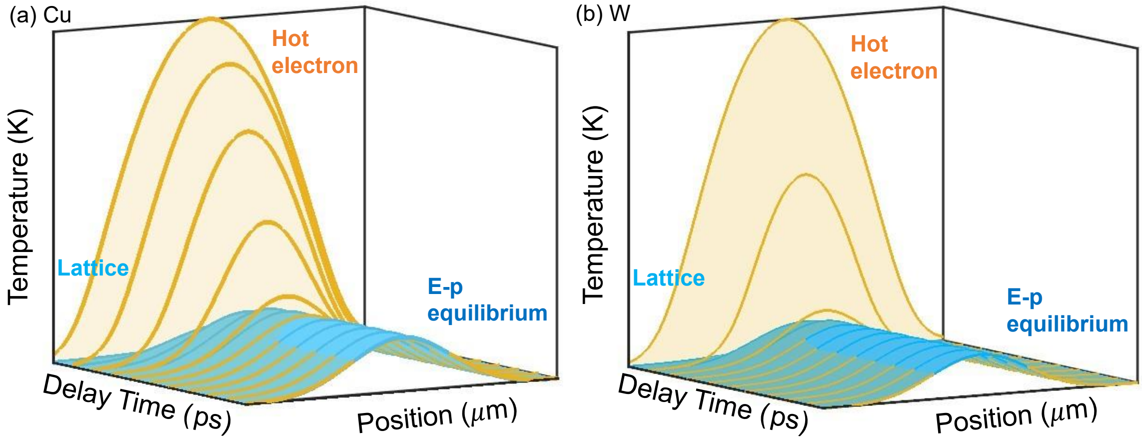

Figure S8: 3D visualization of the electron and phonon temperature profiles varying in space and time for (a) Cu and (b) W obtained from two-temperature picture. The yellow region indicates the photo-excited electron region while the cyan region indicates the lattice subsystem.

We analyze the gaussian profiles for electron-phonon coupling term ($A_1 = T_\mathrm{e} - T_\mathrm{p}$) and the electron heat diffusion term ($A_2 = -(\kappa_\mathrm{e}/G)\,\nabla^2 T_\mathrm{e}$) at different times for both Cu and W as shown in Fig. S9. At 0.3 ps, we observe a significant disparity between A_1 and A_2 for both Cu and W. The notably higher values of A_1 for Cu than W indicates that electrons in Cu attain much higher temperature than W. With the progression of time, electrons begin to dissipate heat to the phonons, leading to a considerable decrease in electron temperature. For Cu, this heat dissipation becomes evident at approximately 5 ps, causing the peak of A_1 to shift away from the center and broadening the temperature profile. In contrast, this phenomenon occurs at around 2.5 ps for W, indicating a rapid heat dissipation process from electrons to phonons. the higher electron-phonon mass enhancement factor in W, highlighted in the main text, accounts for this behavior. At 10 ps, we observe, complete thermalization between electrons and phonons for Cu and W. During this stage, phonon temperature exceeds electron temperature, resulting in the negative values of A1 at the center. At this stage, A_1 and A_2 counterbalance each other leading to a slow and steady diffusion of the electrons. Notably, the magnitude of both A_1 and A_2 are higher for Cu than W, leading to a higher electron diffusion rate in Cu, as shown in Figs. 2a and 2d of the main text.

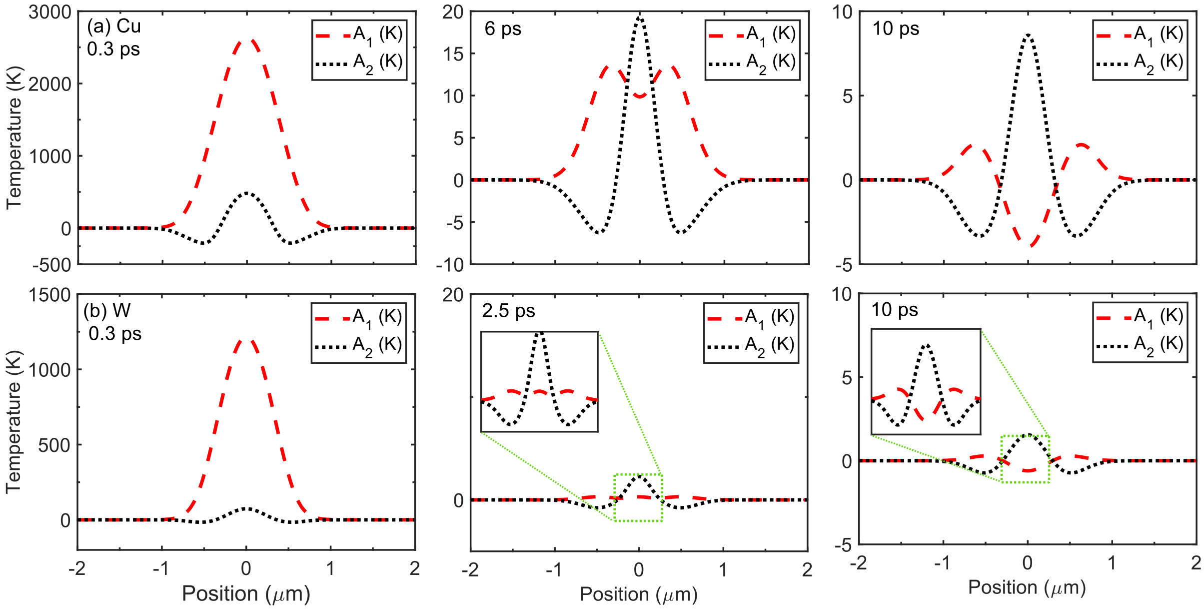

Figure S9: Temperature profiles of A_1 and A_2 at different times for (a) Cu and (b) W. The specific time labelled in the figures indicate the time immediately after laser excitation, intermediate time when the electrons and the phonons have reached equilibrium and long after the electrons have completely thermalized with phonons.

We plot the electron and phonon temperatures at zero pump-probe time delay as obtained by solving Eq. 2 for copper. The maximum electronic temperature reached is ~3,300 K when the copper film is irradiated with a pump fluence of 1.6 mJ cm^{-2}. The rise in phonon temperature is slower that the electron temperature and the electron-phonon temperature equilibrates at ~4 ps. The shrinking of the temperature profile occurs at ~2 ps for copper, which is before the time regime when equilibrium is reached between the electrons and phonons.

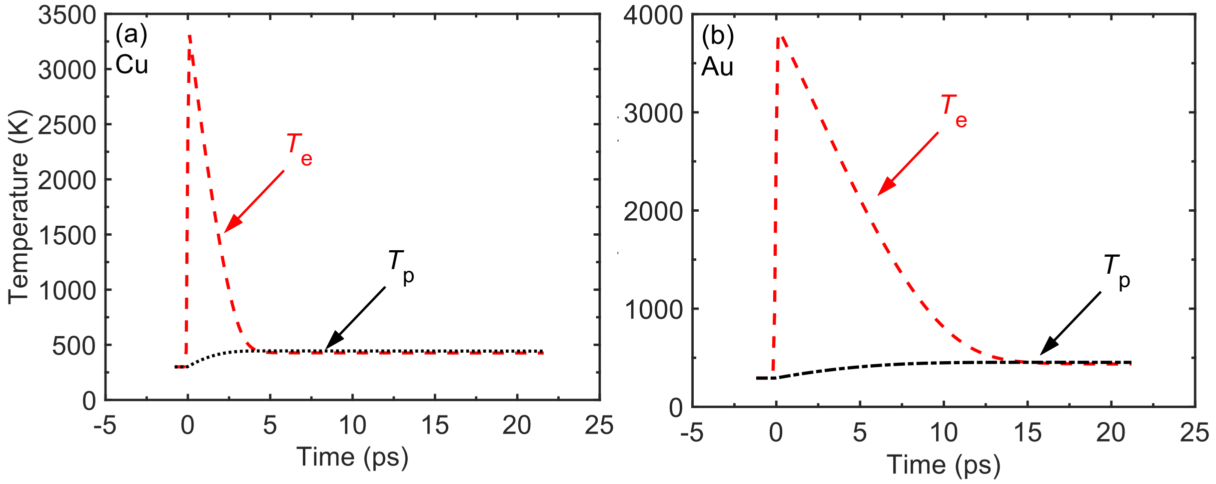

Figure S10: Comparison of electron and phonon temperature profiles obtained for (a) copper and (b) gold. The temperature profiles are obtained using the room-temperature coupling factor of G = 8 × 10^{16} W m^{-3} K^{-1} for copper and G = 2.2 × 10^{16} W m^{-3} K^{-1}.

S6. First-principles calculations: Methodology

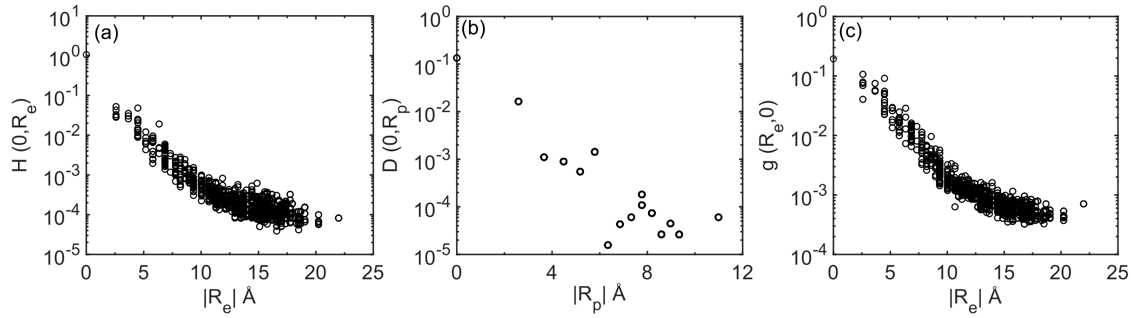

Figure S11: Spatial degeneration of (a) the Hamiltonian, (b) the dynamical, and (c) the electron-phonon matrix element g(R$_e$, 0) at room temperature.

We calculate the Eliashberg spectral function $\alpha^2F(\omega)$ for different metals at room temperature from our density functional perturbation theory (DFPT) calculations as shown in Fig. S12. We also calculate the corresponding mass enhancement factor (λ), an indicator of electron-phonon coupling for each of these metals. From our calculations, we find that the noble metals have relatively low values of λ, in comparison to other metals. Among the metals for which calculations are presented here, Nb has the highest λ, which is also reflected in the Λ of the electrons for Nb. The $\alpha^2F(\omega)$ (ω) calculation also gives an insight into the maximum frequency of vibration for phonons for each of these metals. Overall, the calculated λ matches with prior first-principles calculation and provides confidence in our calculations of the volumetric electron-phonon coupling factor G. The results for the calculations of G based on our first-principles determined eDOS and λ are shown in Fig. S16, which plots G as a function of electron temperature.[14,16]

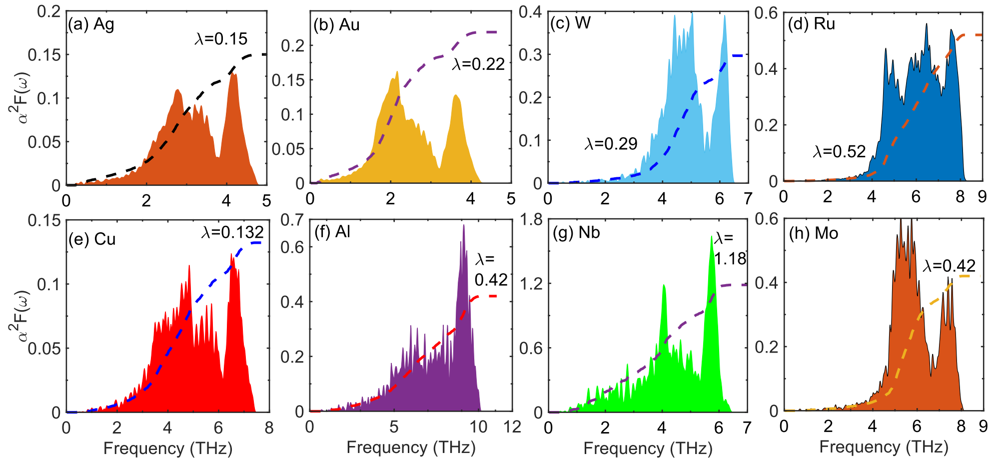

Figure S12: Calculated Eliashberg spectral function $\alpha^2F(\omega)$ for (a) Ag, (b) Au, (c) W, (d) Ru, (e) Cu, (f) Al, (g) Nb and (h) Mo at room temperature. The dashed lines indicate the corresponding mass enhancement parameter, λ.

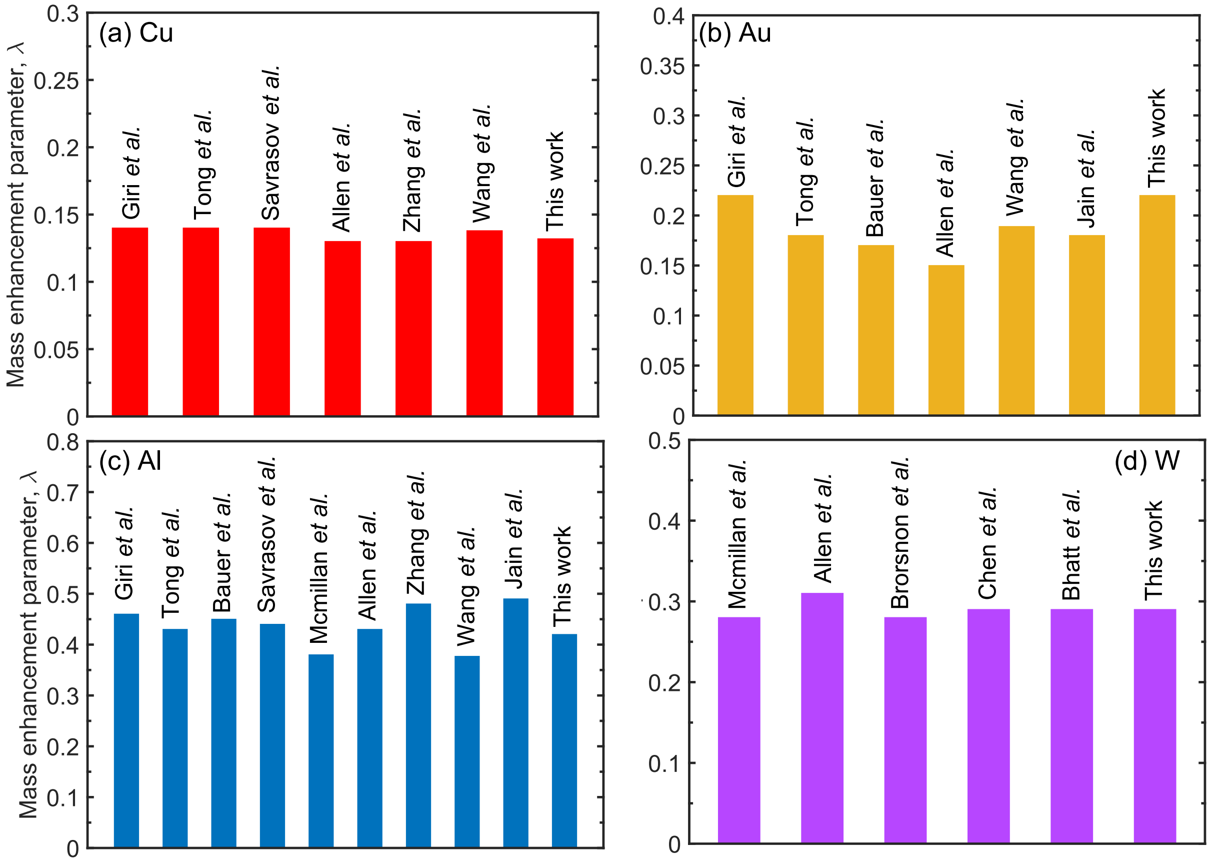

Figure S13: Comparison of our DFT calculated mass enhancement parameter, λ, with prior calculations for (a) Cu, (b) Au, (c) Al and (d) W. For Cu, we compare our results with Giri *et* *al.*,[14] Tong *et al.*,[7] Savrasov *et al.*,[17] Allen *et al.*,[18] Zhang *et al.*,[19] and Wang *et al.*,[20]. For Au, we compare our results with Giri *et al.*,[14], Tong *et al.*,[7] Bauer *et al.*,[21] Allen *et al.*,[18] Wang *et al.*,[20] and Jain *et al.*[22] For Al, we compare our results with Giri *et al.*,[14] Tong *et al.*,[7] Bauer *et al.*,[21] Savrasov *et al.*,[17] Mcmillan *et al.*[23] Allen *et al.*,[18] Zhang *et al.*,[19] Wang *et al.*,[20] and Jain *et al.*[22] For W, we compare our results with Mcmillan *et al.*[23], Allen *et al.*,[18] Brorsnon *et al.*,[24] Chen *et al.*, [8] and Bhatt *et al.*[25]

We compare our first-principles calculated mass enhancement parameter, λ, with prior DFT calculations and empirical measurements as shown in Figure S13. Overall, our calculations are in good agreement with these calculations for all four metals.

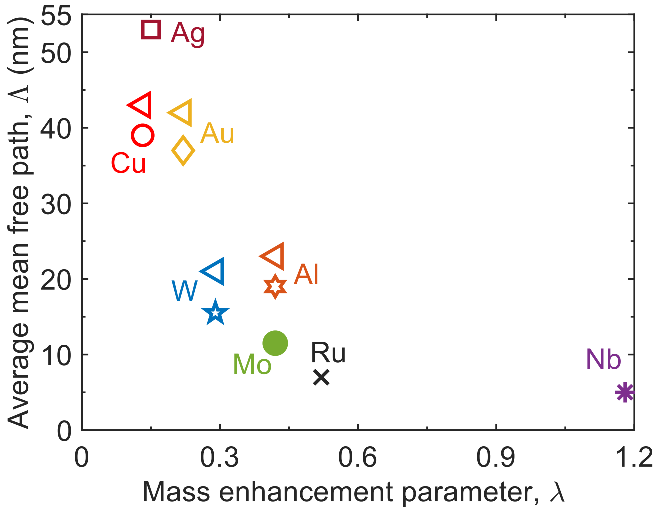

Figure S14: Variation of average mean free path (Λ) at the Fermi energy with mass enhancement parameter, λ, for different metals. The triangular symbols represent the Λ obtained from our experimental measurements.

Finally, we plot the variation of mean free path (Λ) with mass enhancement parameter, λ, that describes the strength of electron-phonon coupling for the different metals. Our calculations and measurements show that the mean free path of the noble metals is distinctly higher than other metals with their λ significantly lower than other transition and free electron metals. While it cannot be said that electron-phonon coupling strength is the single determining factor for the Λ, it has a massive influence on Λ for the metals as revealed by our first-principles calculation and pump-probe measurements.

S7. Calculation of electronic density of states

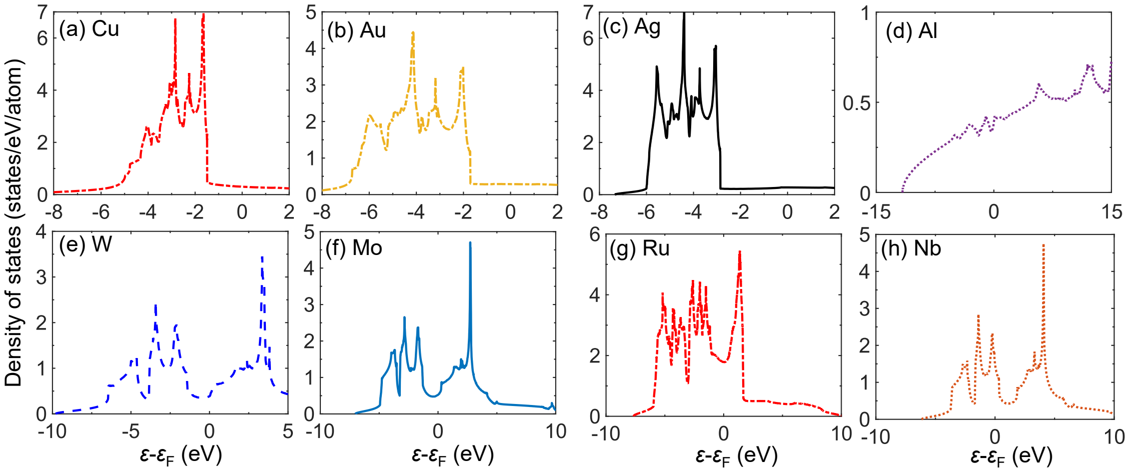

Figure S15: Calculated electronic density of states for (a) Cu, (b) Au, (c) Ag, (d) Al, (e) W, (f) Mo, (g) Ru and (h) Nb. The calculated density of states gives an insight into the electronic configuration of these metals.

We calculate the electronic density of states (eDOS) for different metals with Quantum Espresso using tetrahedron method with k-point grid of 50 × 50 × 50. Fig.S14 shows our results for the eDOS for all metals. The noble metals have noticeable high density region associated with *d*-bands located at ~2-4 eV below the Fermi level in their eDOS.[1] In contrast, Al exhibits a typical free-electron-like eDOS. Similar to the noble metals, our calculations show that Al also has relatively flat DOS near the Fermi level. All other metals (W, Nb, Ru, Mo) have high density peaks of *d*-bands close to the Fermi level in comparison to the noble metals. Overall, our eDOS calculations, are in close agreement with prior calculations.[11,26–29]

S8. Calculation of electron-phonon scattering rate

Figure S16: Calculated scattering rates of electrons due to electron-phonon scattering for (a) Ag, (b) Cu, (c) Au (d) Al, (e) W, (f) Mo, (g) Ru and (h) Nb at room temperature. We derive the average Λ of electrons at Fermi level from the calculated scattering rates and the Fermi velocities (i-p).

We calculate the electron-phonon scattering rate of different metals at room temperature due to electron-phonon scattering from our parameter free DFPT calculations as shown in Fig. S15. From the calculated scattering rates, we calculate the average Λ of electrons for these metals at Fermi level. We find that the noble metals have significantly higher Λ is, e.g. Ag~53 nm, Cu~39 nm, Au~37 nm in comparison to other metals e.g. Al~19.5 nm, W~15.5 nm, Nb~6 nm. Our DFPT calculated Λ are in good agreement with the values reported in Ref. S6-8 and further validate our experimentally measured Λ for Cu, Au, Al and W.

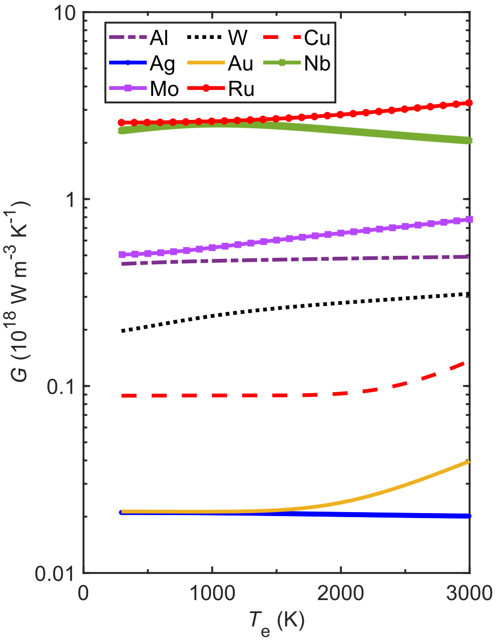

Figure S17: Calculated volumetric electron-phonon coupling factor, $G(T_e)$ for different metals. The calculation is carried out by utilizing electronic density of states and the second moment of phonon spectrum, $\langle\omega^2\rangle$, and the mass enhancement parameter λ.

S9. Calculation of phonon dispersion

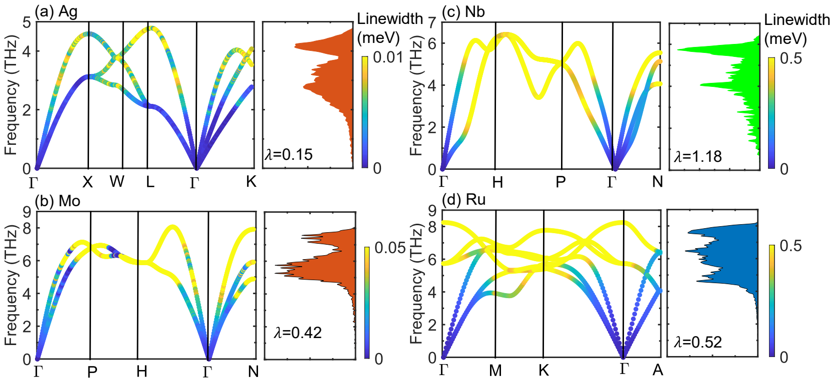

Figure S18: Phonon dispersions calculated along the high symmetry directions for (a) Ag, (b) Mo, (c) Nb and (d) Ru using density functional perturbation theory. The color intensities of the phonon branches indicate the linewidths due to electron-phonon interactions. The corresponding mass enhancement parameters, λ, and the Eliashberg spectral functions, $\alpha^2F(\omega)$, are also shown.

We calculate the phonon dispersions along the high symmetry lines for Ag, Mo, Nb and Ru using DFPT as shown in Fig. S17. The color intensities are related with linewidths of the phonon branches due to electron-phonon interactions. We also show the corresponding mass enhancement parameter, λ along with the Eliashberg spectral function, $\alpha^2F(\omega)$, which represents the overall strength of the electron-phonon coupling in the metals. Similar to Au and Cu, Ag also has weak electron-phonon coupling as compared to other metals. Our calculations show that Nb has the highest electron-phonon coupling strength which is reflected on the Λ which is significantly low compared to noble metals. The phonon dispersion of Ru shows the presence of optical phonons, which is due to the consideration of two atoms for the hexagonal crystal structure during the DFPT calculations.

References

[1] A. Block, M. Liebel, R. Yu, M. Spector, Y. Sivan, F. J. García De Abajo, N. F. Van Hulst, *Sci. Adv.* 2019, *5*, eaav8965.
[2] M. Segovia, X. Xu, n.d.
[3] P. Karna, M. S. B. Hoque, S. Thakur, P. E. Hopkins, A. Giri, *Nano Lett.* 2023, *23*, 491.
[4] C. Thomsen, H. T. Grahn, H. J. Maris, J. Tauc, *Phys. Rev. B* 1986, *34*, 4129.
[5] J. Crank, *The Mathematics of Diffusion*, Clarendon Press, Oxford, 1976.
[6] D. Gall, *Journal of Applied Physics* 2016, *119*, 085101.
[7] Z. Tong, S. Li, X. Ruan, H. Bao, *Phys. Rev. B* 2019, *100*, 144306.
[8] Y. Chen, J. Ma, S. Wen, W. Li, *npj Comput Mater* 2019, *5*, 98.
[9] P. E. Hopkins, J. C. Duda, B. Kaehr, X. Wang Zhou, C.-Y. Peter Yang, R. E. Jones, *Applied Physics Letters* 2013, *103*, 211910.

[10] P. E. Hopkins, L. M. Phinney, J. R. Serrano, *Journal of Heat Transfer* 2011, *133*, 044505.
[11] Z. Lin, L. V. Zhigilei, V. Celli, *Phys. Rev. B* 2008, *77*, 075133.
[12] C. Kittel, *Introduction to Solid State Physics*, Wiley, Hoboken, NJ, 2005.
[13] S. Sæther, M. F. Erichsen, S. Xiao, Z. Zhang, A. Lervik, J. He, *AIP Advances* 2022, *12*, 065301.
[14] A. Giri, M. V. Tokina, O. V. Prezhdo, P. E. Hopkins, *Materials Today Physics* 2020, *12*, 100175.
[15] Y. Chen, J. Ma, W. Li, *Phys. Rev. B* 2019, *99*, 020305.
[16] P. Karna, A. Giri, *Phys. Rev. B* 2023, *107*, 094301.
[17] S. Y. Savrasov, D. Y. Savrasov, *Phys. Rev. B* 1996, *54*, 16487.
[18] P. B. Allen, *Phys. Rev. B* 1987, *36*, 2920.
[19] J. Zhang, R. Qin, W. Zhu, J. Vorberger, *Materials* 2022, *15*, 1902.
[20] Y. Wang, Z. Lu, X. Ruan, *Journal of Applied Physics* 2016, *119*, 225109.
[21] R. Bauer, A. Schmid, P. Pavone, D. Strauch, *Phys. Rev. B* 1998, *57*, 11276.
[22] A. Jain, A. J. H. McGaughey, *Phys. Rev. B* 2016, *93*, 081206.
[23] W. L. McMillan, *Phys. Rev.* 1968, *167*, 331.
[24] S. D. Brorson, A. Kazeroonian, J. S. Moodera, D. W. Face, T. K. Cheng, E. P. Ippen, M. S. Dresselhaus, G. Dresselhaus, *Phys. Rev. Lett.* 1990, *64*, 2172.
[25] N. Bhatt, P. Karna, S. Thakur, A. Giri, *Phys. Rev. Materials* 2023, *7*, 115001.
[26] A. Giri, M. V. Tokina, O. V. Prezhdo, P. E. Hopkins, *Materials Today Physics* 2020, *12*, 100175.
[27] V. Recoules, J. Clérouin, G. Zérah, P. M. Anglade, S. Mazevet, *Phys. Rev. Lett.* 2006, *96*, 055503.
[28] S. Wen, J. Ma, A. Kundu, W. Li, *Phys. Rev. B* 2020, *102*, 064303.
[29] T. Zhang, G. Y. Guo, *Phys. Rev. B* 2005, *71*, 214442.